PCCP

Dynamic Article Links

Cite this: *Phys. Chem. Chem. Phys.*, 2012, **14**, 15361–15368

www.rsc.org/pccp

PAPER

Morphology and nanostructure of CeO_2(111) surfaces of single crystals and Si(111) supported ceria films

H. H. Pieper,[a] C. Derks,[a] M. H. Zoellner,[b] R. Olbrich,[a] L. Tröger,[a] T. Schroeder,[bc] M. Neumann[a] and M. Reichling*[a]

Received 6th August 2012, Accepted 14th September 2012
DOI: 10.1039/c2cp42733h

The surface morphology of CeO_2(111) single crystals and silicon supported ceria films is investigated by non-contact atomic force microscopy (NC-AFM) and Kelvin probe force microscopy (KPFM) for various annealing conditions. Annealing bulk samples at 1100 K results in small terraces with rounded ledges and steps with predominantly one O–Ce–O triple layer height while annealing at 1200 K produces well-ordered straight step edges in a hexagonal motif and step bunching. The morphology and topographic details of films are similar, however, films are destroyed upon heating them above 1100 K. KPFM images exhibit uniform terraces on a single crystal surface when the crystal is slowly cooled down, whereas rapid cooling results in a significant inhomogeneity of the surface potential. For films exhibiting large terraces, significant inhomogeneity in the KPFM signal is found even for best possible preparation conditions. Applying X-ray photoelectron spectroscopy (XPS), we find a significant contamination of the bulk ceria sample with fluorine while a possible fluorine contamination of the ceria film is below the XPS detection threshold. Time-of-flight secondary ion mass spectroscopy (TOF-SIMS) reveals an accumulation of fluorine within the first 5 nm below the surface of the bulk sample and a small concentration throughout the crystal.

I. Introduction

High oxygen mobility and the oxygen storage capability of CeO_2 give rise to its remarkable catalytic properties.[1] The understanding of elementary catalytic processes like, for instance, the water gas shift reaction[2–4] and redox reactions in the three-way catalyst[5] requires a basic knowledge of ceria surface structures and defect formation on ceria surfaces. While the appearance of oxygen vacancies and low coordinated surface sites at step edges as well as water adsorption on CeO_2(111) have been the topic of recent investigations,[6–8] here we focus on the ultra-high vacuum preparation of (111) surfaces of cerium dioxide as the predominant facet occurring in nanocrystalline CeO_2.[9,10] The issue of surface preparation is not only important for surface chemistry but also plays an important role in the understanding of the nucleation and dispersion of metal nanoparticles on the CeO_2(111) surface.[11–14]

The goal of the present paper is to explore preparation conditions for CeO_2(111) surfaces with a well-defined equilibrium morphology, large atomically flat terraces and a low density of defects. The surface topography and the detailed nanoscopic structure of the CeO_2(111) surface are investigated by non-contact atomic force microscopy (NC-AFM)[15] while Kelvin probe force microscopy (KPFM)[16] reveals features related to surface polarization and charging.[17] X-ray photoelectron spectroscopy (XPS) and time-of-flight secondary-ion mass spectroscopy (TOF-SIMS) are employed to detect and quantify a fluorine contamination present in bulk ceria samples.

Ceria single crystals with dimensions of several millimeters or larger are very rare as they can only be prepared by intricate methods like flux growth[18,19] or cold crucible induction melting.[20] Therefore, we have been seeking for alternative ceria systems exhibiting the properties of bulk ceria. There is now a plethora of ceria thin and ultra-thin film systems grown on metal substrates available,[21–32] however, their properties exhibit significant deviations from the bulk behavior. The only system we consider as a possibly adequate replacement for bulk samples are thick films that can be grown in high quality on Si(111) substrates.[33] Furthermore, the growth of CeO_2 on silicon is interesting for applications in semiconductor technology as its high dielectric constant[34] and a lattice mismatch of only 0.35% to silicon[35] make ceria thin films a promising material for advanced microelectronics applications.[33,36] Also in this context, surface morphology, nanostructure and defects are of relevance. Here we investigate bulk ceria and ceria films with a thickness of 180 nm grown on Si(111) and directly compare results of similarly prepared systems.

[a] *Fachbereich Physik, Universität Osnabrück, Barbarastr. 7, 49076 Osnabrück, Germany. E-mail: reichling@uos.de*
[b] *IHP, Im Technologiepark 25, 15236 Frankfurt (Oder), Germany*
[c] *BTU Cottbus, Konrad-Zuse-Str. 1, 03046 Cottbus, Germany*

II. Experimental methods

Experiments are performed in an ultra-high vacuum (UHV) system operated at a base pressure in the low 10^{-10} mbar range and at room temperature with a commercial NC-AFM system, which has been modified to obtain a better quality.[37] Silicon cantilevers (p-doped, 0.015 Ω cm specific resistance) with an eigenfrequency of about 300 kHz and a stiffness of about 30 N m^{-1} (Type NCH, Nanoworld AG, Neuchâtel, Switzerland) are used for high resolution NC-AFM studies and simultaneous KPFM measurements. Cantilevers are Ar^+-sputtered prior to their use in experiments to remove the native oxide layer and to remove tip contamination. KPFM measurements are performed in the frequency modulation mode,[38] where the bias voltage is the sum of a DC voltage V_{DC} and a sinusoidally modulated AC voltage (0.5 V RMS-amplitude, 1323 Hz modulation frequency). KPFM images display the inverse of the regulated value V_{DC} and directly represent the distribution of charges or dipoles on the surface of the insulating crystal.[39] A positive charge is represented by a bright shading while a negative charge is coded dark.[40]

X-ray photoelectron spectroscopy (XPS) and time-of-flight secondary ion mass spectroscopy (TOF-SIMS) experiments are also performed at room temperature in separate vacuum systems after transfer of the sample through the ambient atmosphere. XPS spectra are recorded using a PHI 5600ci multi-technique spectrometer (Physical Electronics, Chanhassen, MN, USA) with monochromatic Al K_α radiation ($h\nu$ = 1486.6 eV) of 0.3 eV FWHM bandwidth. The pass energy of the monochromator is set to 187.85 eV yielding a resolution of 0.44 eV. All spectra are obtained using a 400 μm diameter analysis area. During the measurements, the pressure in the main chamber is kept at about 10^{-9} mbar. TOF-SIMS measurements are performed using a TOF.SIMS 5 spectrometer (ION-TOF GmbH, Münster, Germany) with different ion beams in alternating sputtering and analyzing cycles. A square with a side length of 300 μm is etched by cesium sputtering (1 keV) and subsequently its center (100 μm side length) is analyzed by bismuth ions (25 keV). For calibration purpose, a silicon supported ceria film with a thickness of 180 nm undergoes this procedure for 30 min. The steep rise in the silicon signal by four orders of magnitude after a certain sputtering time indicates the boundary between the ceria film and the silicon substrate. Assuming the sputtering depth increases linearly with time and the sputter yield is the same for different ceria samples, this provides a depth calibration for the TOF-SIMS measurements performed on the ceria single crystal.

The CeO_2(111) surface is usually prepared by multiple cycles of Ar^+-ion sputtering and annealing in UHV where the obtained surface morphology strongly depends on the preparation parameters.[41] Recent investigations revealed a strong dependence of the morphology on the annealing time.[42] In these experiments, the time to reach the desired temperature has been chosen to be as short as 40 s.[43] We have tried several preparation procedures, and developed a standard procedure involving much slower heating.

To put our findings into perspective, here we provide a description in very detail. A single crystal of ceria with dimensions of about 8 × 2 × 0.5 mm^3 (Commercial Crystal Laboratories, Naples, FL, USA) is mechanically polished by the manufacturer and after transfer to the UHV initially cleaned by four sputter–annealing cycles using a preparation system described in detail elsewhere.[14] This step is repeated after each transfer to the UHV as well as after experiments that include the deposition of metal clusters. The NC-AFM measurements performed at room temperature start one hour after the end of the final cooling cycle. Large scale NC-AFM imaging (100 nm frame size) reveals that the sample remains clean for about one week. However, after a few days we observe the adsorption of individual water molecules on the sample in high resolution measurements and find that such weak water contamination can completely be removed by one additional sputter–annealing cycle. During their lifetime, samples are used for numerous experiments and undergo many hundreds of complete sputter–annealing cycles. For the first sputter cleaning cycle, Ar^+-ions with an energy of 0.5 keV and an exposure time of 5 min are used. The aim here is to gently clean the crystal and to avoid damage and roughening of the surface. In later sets of experiments, the argon energy is increased to 1.5 keV, to enhance the material removal and yield a perfectly clean surface within one cycle even after metal deposition.

The annealing cycles are done with a resistively heated tantalum foil pressed against the back side of the sample.[14] The applied voltage is linearly ramped, resulting in a slow and monotonic increase and decrease in the surface temperature. This procedure yields a retarded increase in the temperature during the first minutes but a nearly linear temperature ramp with a slope of about 1 K s^{-1} for a temperature interval from 450 K to 1150 K. Finally, the ramp is stopped approximately 30 K below the desired temperature T_{max} and the temperature asymptotically approaches the value T_{max}. During the following 15 minutes, the heating power is slightly re-adjusted so that variations in the sample temperature are limited to ±15 K. Also for cooling, the temperature is ramped down with about the same rate as during heating. This procedure is further on referred to as the *standard procedure* and grants a homogeneous heating of the surface and the minimization of mechanical stress by thermal expansion. For some experiments, we apply a *quenching procedure* that deviates from the standard procedure only by the cooling rate. The heating power maintaining T_{max} is not continuously decreased but instantly switched off. This results in a temperature drop of 560 K within the first minute of cooling.

The ceria film with a thickness of 180 nm is grown on a Si(111) wafer with a 1 nm thick hex-Pr_2O_3 buffer as described in detail elsewhere.[33] The film thickness is determined by X-ray reflection while its crystallinity is verified by X-ray diffraction methods. For NC-AFM investigations, the wafer is cut into pieces of 8 × 2 mm^2 dimensions and mounted on the same sample holder as used for the ceria bulk samples[14] and then transferred to the UHV. The film is prepared in a similar fashion to the bulk sample. The large number of samples cut from the wafer allows a frequent exchange. For preparation cycles the maximum temperature is limited to 1100 K as annealing to higher temperatures results in a destruction of the film presumably initiated by a structural transformation of the buffer layer.

III. Results

Fig. 1(a) and (b) show the typical morphology as revealed by NC-AFM imaging of a bulk sample subjected to the standard procedure with a maximum temperature of 1100 K maintained for 15 min. For this crystal, there was a slight misorientation between the crystal cut and the (111) plane resulting in a vicinal surface with a large number of preferentially oriented ledges and terraces descending from the top left to the bottom right. The ledges appear rounded and their separation is found to hardly exceed 20 nm. Frequently observed structures are irregularly shaped pits with a depth of one O–Ce–O triple layer (TL) marked by dashed circles and screw dislocations showing up as step edges emerging on a terrace as the one marked by a circular arrow. As evident from the height distribution shown in Fig. 1(c), step heights mostly correspond to one (64%) or two (31%) triple layers. The method of image analysis and generation of the step height distribution is described in detail in Appendix A. The surface shown in Fig. 1(b) is the result of applying only one preparation cycle after the introduction of the new sample into the vacuum chamber. This results in clean terraces but remaining contamination at step edges motivate the application of further preparation cycles.

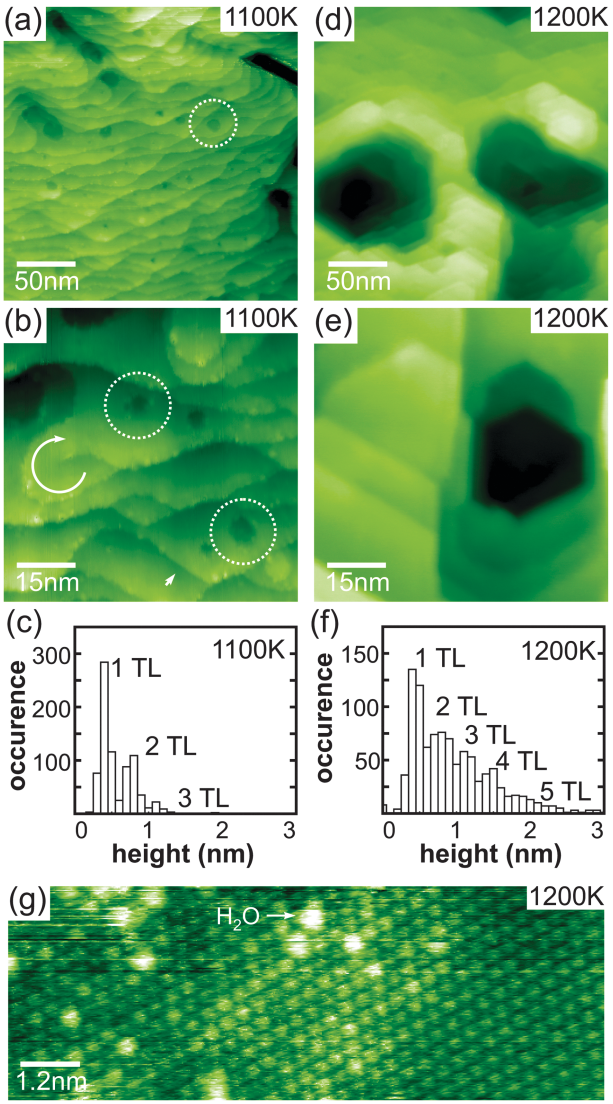

Fig. 1 Morphology and surface atomic structure of the (111) surface of a CeO_2 single crystal prepared at different maximum annealing temperatures. Rounded ledges are formed for annealing at 1100 K (a, b) while straight ledges with structures following a hexagonal motif are formed for annealing at 1200 K (d, e). The diagrams (c) and (f) show the step height distributions extracted from topography images by a procedure described in Appendix A. (g) Atomically resolved image of CeO_2(111) exhibiting patches of enhanced atomic contrast of yet unknown origin and adsorbed water molecules but no surface or sub-surface vacancies.[7]

For better cleaning and the formation of larger terraces and more regular step edges, the preparation temperature is increased to 1200 K. The resulting morphology shown in Fig. 1(d) and (e) is dominated by hexagonally shaped hillocks and adjacent holes. The irregularly shaped pits on terraces with TL depth have disappeared and we observe the formation of straight step edges. Hexagonal structures are formed by step bunching, while the surface roughness increases drastically. The height distribution shown in Fig. 1(f) is much broader than for the surface prepared at lower temperature and exhibits a quantization of step height according to 312 pm for the elementary TL step; only one-third of the steps have a height of one TL. We speculate that the formation of these structures that are closer to a thermodynamic equilibrium state than results for lower preparation temperatures is kinetically favored by screw dislocations that are found in large numbers all over the surface. The magnified image of Fig. 1(e) shows steps in more detail and demonstrates their cleanliness and straight alignment with only very few kink. Their alignment is parallel to the $\langle\bar{1}10\rangle$ family of surface directions as reported earlier.[8]

For both preparation temperatures, terraces appear atomically flat and free of contaminants. As seen in Fig. 1(g), however, individual water molecules appear during days after surface preparation.[44] The regular hexagonal array of bright spots resolved at the atomic scale is interpreted as the anion sublattice.[6] The only surface irregularities frequently observed immediately after preparation are patches or lines of surface atoms with a slightly enhanced contrast as also apparent in Fig. 1(g) where the origin of this phenomenon is not yet known. Oxygen vacancies[7] or other surface defects[45] are only very rarely observed under the preparation conditions described here.

To understand the formation of surface structures and defects resulting from different preparation procedures in more detail, we recall that the surface structure is generally the result of a complex interaction of thermodynamically and kinetically controlled processes where the rate constant k of the latter is governed by the Arrhenius equation

$$k = A \exp(-E_a/k_B T)$$

with the activation barrier E_a, the Boltzmann constant k_B and the pre-exponential factor A. This is likewise relevant for the formation of regular or irregular step structures as for the formation of point defects. Regarding point defects, the main mechanism in a reducible oxide like ceria is the formation of

bulk and surface vacancies.[7] By applying a slow temperature ramp while cooling down the sample during the standard preparation, the surface can relax and finally solidify in a thermodynamically rather stable state and the healing of point defects is kinetically not hindered. The result is a surface that appears as rather perfect in its nanostructure and free of point defects and defect agglomerates. The fact that the above mentioned slight surface irregularities appear in patches with a well ordered atomic structure even after applying the standard procedure point to their nature as chemical impurities and we speculate that they might be fluorine ions on oxygen substitutional sites as fluorine is a contamination present in the crystal as verified below.

To elucidate kinetic effects in more detail, we study the impact of quenching the crystal at the end of the preparation cycle on the appearance of step edges and reveal quenching-induced near-surface defects that cannot be seen in topography on a large scale but appear in KPFM images. Fig. 2 is a comparison of results obtained by the standard preparation and by quenching where simultaneously recorded images for the topography (z) and the surface potential (Φ) are shown. Topography images from frames (a) and (b) in their basic structure closely resemble those from Fig. 1(d) and (e), however, KPFM reveals additional structures, namely the different polarity of two types of step edges. In the hexagonal step structures this appears as a pronounced alternating bright and dark (mostly less pronounced) contrast of the edges that might be related to electronic structure effects at step edges of different type reported for a (111) oriented ceria thin film.[46] We recently observed a similar phenomenon on cleaved CaF_2(111) surfaces,[40] however, we anticipate that the origin of the contrast is different for CaF_2 where anti-Frenkel disorder with pairs of vacancies and F^- interstitials is dominant while CeO_2 is a reducible oxide where the excess charge left by vacancies is transferred to the cation lattice. While we leave a detailed interpretation of KPFM contrast formation to future studies, here we point out that terraces exhibit a rather uniform potential without any significant local contrast variations.

The surface morphology obtained by quenching the sample as shown in Fig. 2(c) and (d) on first sight resembles the results for the standard preparation. However, as a detail difference, we observe a higher density of somewhat less regular steps and as an additional structural element, straight lines along the [$\bar{1}$10] direction (labeled by pairs of white arrows). These lines are topographic features that do not show up in the surface potential image. We further note that they cannot be regular ledges as they cross other ledges. We regard them as two dimensional defects like glide planes formed as a result of mechanical stress.[47,48] KPFM reveals a predominant positive potential at step edges as for the standard preparation sample surface, however, we find patches with a relatively strong negative potential (dark) irregularly spread over the surface. The magnified KPFM image from Fig. 2(d) reveals that these patches (marked by dotted circles) are located on terraces and are not related to step edges. NC-AFM images on this scale, however, exhibit atomically flat terraces pointing to sub-surface polarization or charges as the origin of the irregularities.

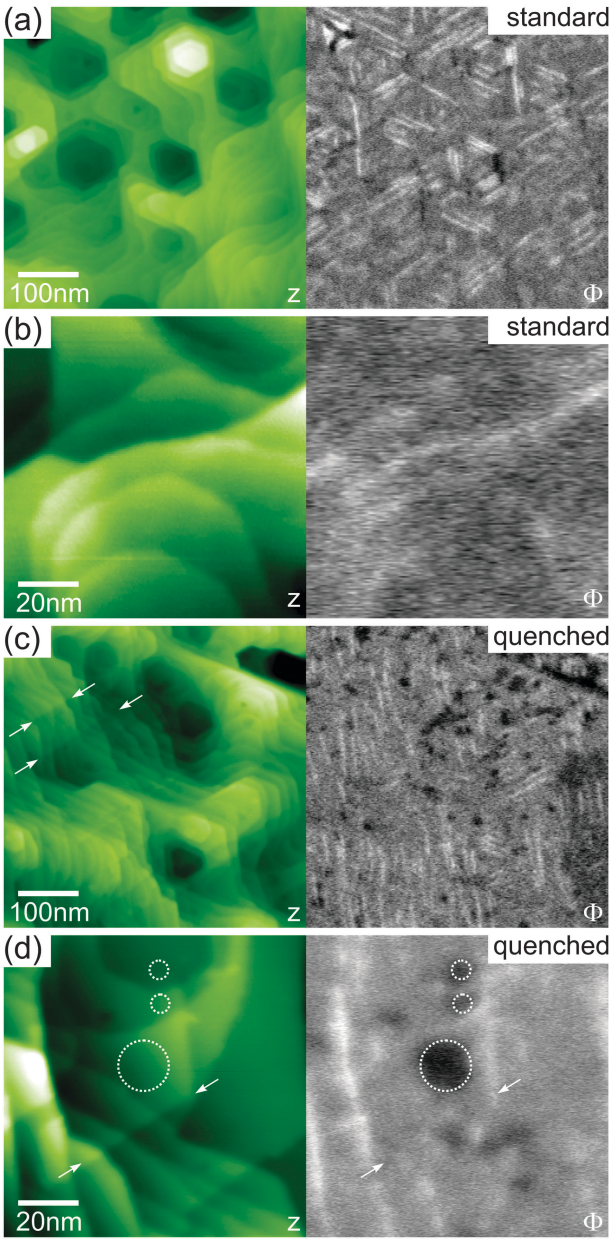

Fig. 2 Topography (z) and surface potential (Φ) for the (111) surface of a CeO_2 single crystal prepared by the standard procedure involving annealing up to 1200 K with a slow temperature ramp (a, b) and for a preparation involving quenching the crystal (c, d). Paired arrows point to line defects while dotted circles mark defects that are not discernible in the surface topography but appear in the surface potential. The grey scale of the potential images ranges from 700 mV (black) to 1200 mV (white) for all images.

Fig. 3 is a comparison of preparation results for the crystal and a film heated to a temperature of 1100 K for 15 min following the standard procedure. The resulting morphology of the film is comparable to the one observed for the single crystal. Top terraces are decorated by hexagonal islands with straight step edges while other ledges with an overall preferential direction along $\langle\bar{1}10\rangle$ are mostly rounded with the steps having a predominant height of one TL. The width of terraces on the film exceeds the terrace width observed on the bulk crystal by one order of magnitude and there is a distinct difference in the

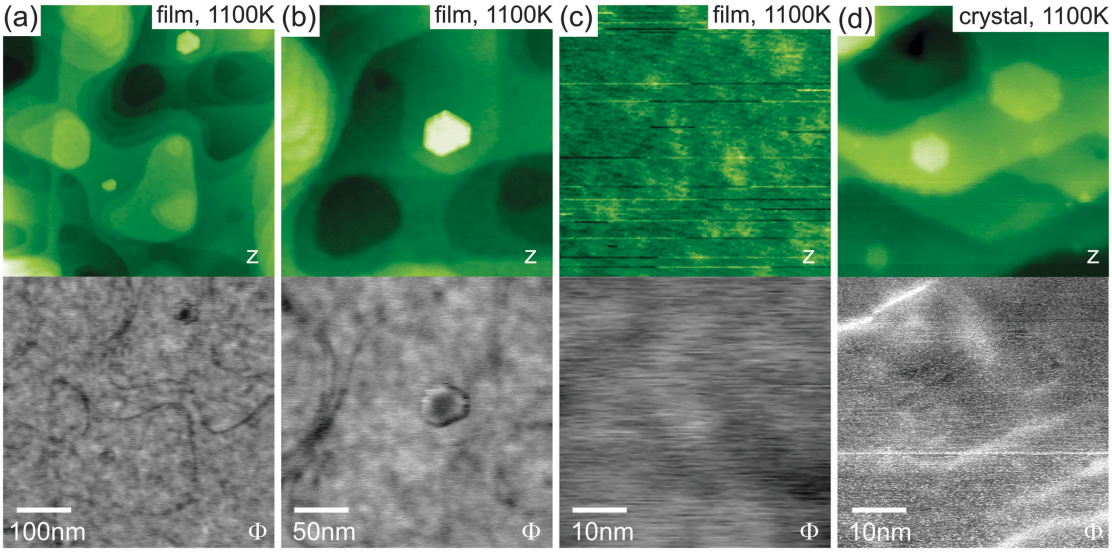

Fig. 3 Topography (z) and surface potential (Φ) for the (111) surface of a CeO_2 film prepared at 1100 K in comparison to respective results for a single crystal. On a large scale (a, b), the shape of step edges resembles the one observed for the likewise prepared single crystal. The surface potential, however, exhibits a strongly different contrast at ledges. On a smaller scale (c) terraces appear more inhomogeneous in z and Φ for the film than for the single crystal. The grey scale represents a span of 500 mV for all potential images.

local surface potential. Ledges on the film exhibit a negative potential (dark), whereas for single crystals, there is a positive potential (bright). The negative potential is found for all ledges of the film regardless of their detailed structure and direction. Further analysis reveals an inhomogeneity of terraces in both, NC-AFM and KPFM images as the one shown in Fig. 3(b) and (c). While the terraces of the single crystal are atomically flat and homogeneous in their potential (see Fig. 3(d)), the potential and topography of the film exhibits significant variation. Furthermore, we observe that this inhomogeneity rapidly increases as a function of time. Within a few hours, residual gas molecules adsorb on terraces and form larger agglomerates. This is in strong contrast to single crystals that remain clean for much longer times.

To characterize the surface and near-surface chemical composition of the samples, XPS measurements are performed on both, ceria crystals and thin film samples. Survey spectra shown in Fig. 4(a) are exemplary for the as inserted (i) and sputter-cleaned (ii) single crystal and for the as-inserted ceria film (iii). The spectra exhibit the expected peak structures related to cerium, oxygen but also carbon (i and iii) due to the transfer of the sample through ambient air. In spectrum (i), an additional feature points to relicts of experiments involving the deposition of gold on the crystal surface that vanish after sputtering. Surprisingly, we find a considerable amount of fluorine for three different ceria single crystals investigated by XPS where the fluorine F1s peak typically has a height of 10 to 15% of the O1s peak height. Considering the lower sensitivity for oxygen (0.66), compared to fluorine (1),[49] this indicates a fluorine concentration of 7 to 10% within the XPS sampling depth. To investigate whether fluorine is a surface contamination or also present in deeper layers, a series of XPS spectra is taken after 5 minute cycles of sputtering with 0.5 keV Ar^+-ions. After two cycles, carbon and gold contaminations are removed, however, the concentration of fluorine is found to increase what is explained by the removal of previously screening

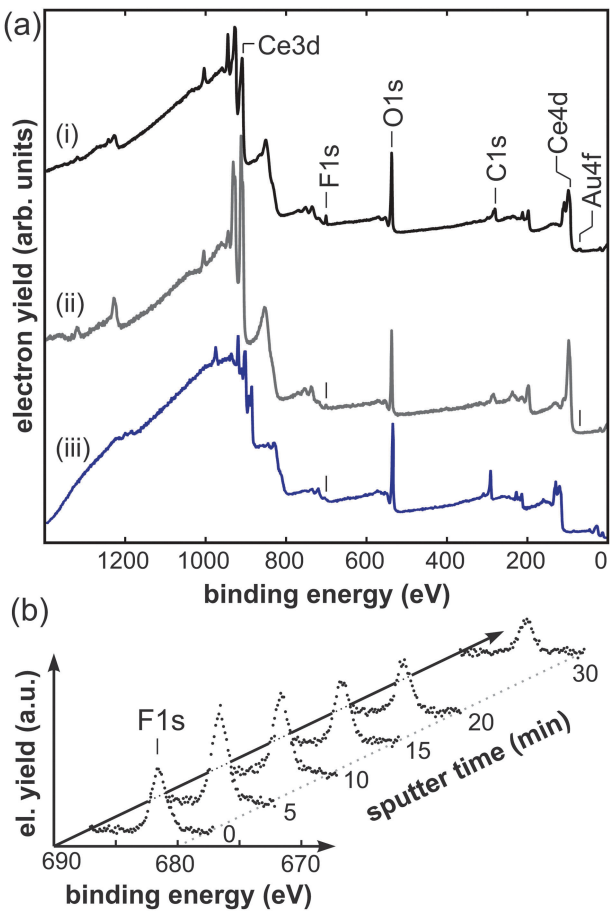

Fig. 4 (a) X-ray photoelectron spectroscopy spectra for the CeO_2 single crystal before (i) and after Ar^+-ion sputtering (ii) and for the untreated CeO_2 film (iii). (b) The evolution of the fluorine F1s peak as a function of the sputter time exhibiting a maximum after the removal of surface contaminants. For better comparability, spectra are normalized to the adjacent background.

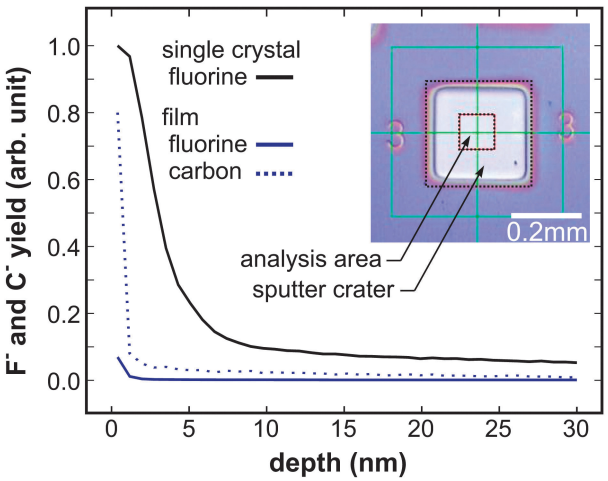

Fig. 5 TOF-SIMS measurements reveal fluorine as a contaminant present in the entire CeO_2 single crystal and an enrichment near the surface. The fluorine concentration for the film is negligible after removing surface contaminants by a few sputter cycles. The inset shows a sputter crater (Cs^+, 1 keV) with a side length of 0.3 mm including the smaller area of SIMS analysis (Bi^+, 25 keV).

surface species. Following sputter cycles performed with an increased ion energy of 1.5 keV for a faster removal of material result in a gradual decrease of the F1s peak as shown in Fig. 4(b). The survey spectrum (ii) in Fig. 4(a) is the one measured after 20 min of such sputter treatment. This yields clear evidence that fluorine is not a surface contamination but present in near-surface layers.

To clarify whether fluorine is present also in the depth of the crystal, XPS measurements are complemented by a TOF-SIMS study. TOF-SIMS allows us to cover a larger depth range and a calibration of the sputter yield that is done here by sputtering the ceria film of known thickness down to the silicon substrate. Fig. 5 shows profiles recorded for the single crystal and the film. At the surface, the fluorine concentration of the single crystal is about one order of magnitude higher than that of the film. Progressing further into the crystal bulk, the concentration decreases and is reduced by a factor of about 20 deep in the bulk. Most of the fluorine is concentrated in a surface layer of about 5 nm thickness. In contrast, the fluorine concentration of the film rapidly decreases parallel to the removal of the carbon surface contaminations and is nearly zero in the inner of the film. As TOF-SIMS provides a most sensitive detection of masses, the clear conclusion to be drawn here is that the ceria crystals contain a significant amount of fluorine throughout the sample with a concentration gradient towards the surface while the ceria film does not contain fluorine in any significant concentration.

IV. Discussion

We introduce a methodology for the preparation of $CeO_2(111)$ surfaces with large, atomically flat terraces and a very low density of atomic size defects. This can perfectly be accomplished by a preparation involving sputter cleaning and annealing to 1100 K for the surface of a ceria single crystal where we obtain terraces with a width of typically 20 nm and terraces that are virtually free of vacancies or other point defects. When increasing the annealing temperature to 1200 K, we additionally obtain equilibrium surface structures with perfectly straight ledges well in accordance with previous preparation results.[8,42] The preparation of a thick ceria film grown on Si(111) yields similar results but terraces are larger by a factor of ten compared to terraces on the single crystal surface. This finding might be the result of a perfect alignment of the silicon crystal with an accuracy of 0.5° in the industrial wafer production process in contrast to the most difficult cutting of the small and very brittle ceria crystal after its crystallographic orientation. We find, however, that the film cannot be annealed to 1200 K without its destruction and the preparation at 1100 K yields a surface that is nominally atomically flat but essentially exhibits a RMS-roughness of 30 pm on terraces and an inhomogeneous surface potential pointing to sub-surface defects. A check of the film for surface vacancies or other point defects is not possible as the atomic scale inhomogeneity of the surface does not allow for atomic resolution imaging. Therefore, it remains a speculation to propose that a different redox behavior of crystal and film is the origin for the apparent differences. The bulk of the single crystal may well be able to supply oxygen for the re-oxidation of a single crystal while the reservoir provided by the film might not be enough. Indeed, a reduction of thin ceria films is observed after annealing in UHV.[26,31,32]

Another remarkable finding is the significant content of fluorine in the single crystals. While the precise origin of the fluorine is unknown, our experiments yield evidence that fluorine is distributed over the entire crystal. We suppose that the diffusion of fluorine is activated by thermal treatment and the surface is a trap for fluorine accumulating there. Halides are known as oxygen substitutional impurities in rare earth oxides[50–54] and in the case of fluorine incorporated into CeO_2, the fluorite structure is maintained and the lattice is not distorted.[55] Substituting O^{2-} by F^- results in a reduction of the crystal in the form of a transformation of Ce^{4+} ions to Ce^{3+} ions. It has been proposed that such reduction suppresses the formation of anion vacancies as observed for chlorine incorporated in CeO_2.[56,57] This might be an explanation that for the crystals we have been using in thousands of experiments we hardly find any vacancy for the standard preparation described here. We can create a measureable number of vacancies only by a very harsh thermal treatment of the crystal and never observed extended line vacancy defects as reported for other crystals prepared in a similar way.[58] The significant fluorine concentration found here probably has an impact on physical and chemical properties of the surface. For example halides have been found to enhance the metal dispersion[56] on ceria and to influence catalytic reactions as in the case of cerium oxychloride where the conversion of ethane and the selectivity to ethylene is enhanced.[56,59] Further investigations involving different types of crystals and advanced NC-AFM imaging and spectroscopy techniques will show whether fluorine can directly be identified as a surface contaminant at the atomic scale and clarify its role in surface adhesion and reactivity.

Appendix A

To derive the distributions of step heights shown in Fig. 1(c) and (f), we pick topography images with a frame width of typically 120 nm as they clearly represent the step structures and terraces with a width of about 20 nm. The quantitative image analysis is performed with a software tool from the Gwyddion[60] software package. In a first step, we compensate for an inclination between the plane of scanning and the (111) surface of the crystal by subtracting a plane from the raw image data so that the height variation in terraces is a minimum and z-positions correspond to absolute height values. A typical result of a topography image after this correction is shown in Fig. A1(a). For each individual terrace, the color does not vary and further protruding terraces are of a brighter color. In a second step, the color coding for the height is altered to pronounce the course of step edges. The brightness is now a sinusoidal function of the height where the number of sine waves is adapted to the presumed number of different step heights present. As a result, a certain color does not correspond to a certain height, but step edges appear very pronounced as they exhibit a strong color change as seen in Fig. A1(b). In a third step of analysis, ledges are manually covered by ellipses with a length of about 10 nm where one half is placed on the upper and the other half on the lower terrace. In that way, the number of ellipses placed along a ledge corresponds to its length. For each ellipse the maximum and minimum height value within its area is determined from the plain-corrected topography data. The histograms in Fig. 1(c) and (f) represent the distribution of height differences within a grouping interval of 0.1 nm. The large number of ellipses placed on many ledges in several images yields statistical significance of the result. However, when applying this procedure, step heights are slightly overestimated, as residual sample misalignment and noise yields errors that always add up when using minimum and maximum values for the analysis within the ellipses. The quantization of step height is, however, not affected by this error that can be assumed to be similar for all terraces.

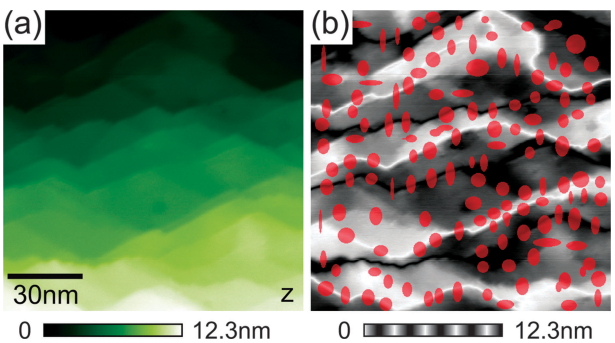

Fig. A1 Topography of a vicinal CeO_2 surface plotted with different color scales. (a) Each color tone corresponds to a specific height. Terraces appear in one tone with only minor variation. (b) A modulated color scale results in the visualization of fine details and a strong enhancement of step edges allowing their easy identification. For a statistical analysis of step height, ledges are covered by ellipses drawn in light red to extract local height information that is analyzed for minimum and maximum values in the selected area.

Acknowledgements

Fruitful discussions with C. Barth on KPFM imaging on insulators are gratefully acknowledged. This work has been supported by the Deutsche Forschungsgemeinschaft via Projects RE 1186/12-1 and SCHR 1123/4-1 as well as the COST Action CM1104.

References

1 A. Trovarelli, C. de Leitenburg, M. Boaro and G. Dolcetti, *Catal. Today*, 1999, **50**, 353.
2 Q. Fu, H. Saltsburg and M. Flytzani-Stephanopoulos, *Science*, 2003, **301**, 935.
3 Q. Fu, S. Kudriavtseva, H. Saltsburg and M. Flytzani-Stephanopoulos, *Chem. Eng. J. (Amsterdam, Neth.)*, 2003, **93**, 41.
4 Q. Fu, A. Weber and M. Flytzani-Stephanopoulos, *Catal. Lett.*, 2001, **77**, 87.
5 H. S. Gandhi, G. W. Graham and R. W. McCabe, *J. Catal.*, 2003, **216**, 433.
6 S. Gritschneder and M. Reichling, *J. Phys. Chem. C*, 2008, **112**, 2045.
7 S. Torbrügge, M. Reichling, A. Ishiyama, S. Morita and O. Custance, *Phys. Rev. Lett.*, 2007, **99**, 056101.
8 S. Torbrügge, M. Cranney and M. Reichling, *Appl. Phys. Lett.*, 2008, **93**, 073112.
9 F. Zhang, Q. Jin and S.-W. Chan, *J. Appl. Phys.*, 2004, **95**, 4319.
10 Z. L. Wang and X. Feng, *J. Phys. Chem. B*, 2003, **107**, 13563.
11 B. H. Li, O. K. Ezekoye, Q. J. Zhang, L. A. Chen, P. Cui, G. Graham and X. Q. Pan, *Phys. Rev. B: Condens. Matter Mater. Phys.*, 2010, **82**, 125422.
12 Y. H. Zhou, J. M. Perket and J. Zhou, *J. Phys. Chem. C*, 2010, **114**, 11853.
13 A. Bruix, F. Nazari, K. M. Neyman and F. Illas, *J. Chem. Phys.*, 2011, **135**, 244708.
14 H. H. Pieper, C. Lammers, L. Tröger, S. Bahr and M. Reichling, *Rev. Sci. Instrum.*, 2012, **83**, 055110.
15 J. V. Lauritsen and M. Reichling, *J. Phys.: Condens. Matter*, 2010, **22**, 263001.
16 W. Melitz, J. Shen, A. C. Kummel and S. Lee, *Surf. Sci. Rep.*, 2011, **66**, 1.
17 C. Barth and C. R. Henry, *Nanotechnology*, 2006, **17**, 155.
18 B. M. Wanklyn, *J. Cryst. Growth*, 1969, **5**, 219.
19 B. M. Wanklyn and B. J. Garrard, *J. Cryst. Growth*, 1984, **66**, 346.
20 E. Ruiz-Trejo, J. D. Sirman, Y. M. Baikov and J. A. Kilner, *Solid State Ionics*, 1998, **113**, 565.
21 U. Berner and K. Schierbaum, *Thin Solid Films*, 2001, **400**, 46.
22 S. Eck, C. Castellarin-Cudia, S. Surnev, M. G. Ramsey and F. P. Netzer, *Surf. Sci.*, 2002, **520**, 173.
23 U. Berner and K. D. Schierbaum, *Phys. Rev. B*, 2002, **65**, 235404.
24 K. Matsumoto, H. Shii, A. Inchinose, H. Adachi, Y. Yoshida, S. Horii, M. Mukaida and K. Osamura, *J. Jpn. Inst. Met.*, 2004, **68**, 730.
25 J. L. Lu, H. J. Gao, S. Shaikhutdinov and H. J. Freund, *Surf. Sci.*, 2006, **600**, 5004.
26 V. Matolín, J. Libra, I. Matolínová, V. Nehasil, L. Sedláček and F. Šutara, *Appl. Surf. Sci.*, 2007, **254**, 153.
27 X. Zhao, S. Ma, J. Hrbek and J. A. Rodriguez, *Surf. Sci.*, 2007, **601**, 2445.
28 R. Wrobel, Y. Suchorski, S. Becker and H. Weiss, *Surf. Sci.*, 2008, **602**, 436.
29 T. Staudt, Y. Lykhach, L. Hammer, M. A. Schneider, V. Matolín and J. Libuda, *Surf. Sci.*, 2009, **603**, 3382.
30 D. C. Grinter, R. Ithnin, C. L. Pang and G. Thornton, *J. Phys. Chem. C*, 2010, **114**, 17036.
31 J. A. Farmer, J. H. Baricuatro and C. T. Campbell, *J. Phys. Chem. C*, 2010, **114**, 17166.
32 P. Luches, F. Pagliuca and S. Valeri, *J. Phys. Chem. C*, 2011, **115**, 10718.
33 M. H. Zoellner, J. Dabrowski, P. Zaumseil, A. Giussani, M. A. Schubert, G. Lupina, H. Wilkens, J. Wollschläger, M. Reichling, M. Bäumer and T. Schroeder, *Phys. Rev. B*, 2012, **85**, 035302.
34 Y. Nishikawa, N. Fukushima, N. Yasuda, K. Nakayama and S. Ikegawa, *Jpn. J. Appl. Phys., Part 1*, 2002, **41**, 2480.

35 T. Inoue, Y. Yamamoto, S. Koyama, S. Suzuki and Y. Ueda, *Appl. Phys. Lett*., 1990, **56**, 1332.
36 J. I. Flege, B. Kaemena, S. Gevers, F. Bertram, T. Wilkens, D. Bruns, J. Bätjer, T. Schmidt, J. Wollschläger and J. Falta, *Phys. Rev. B*, 2011, **84**, 235418.
37 S. Torbrügge, J. Lübbe, L. Tröger, M. Cranney, T. Eguchi, Y. Hasegawa and M. Reichling, *Rev. Sci. Instrum*., 2008, **79**, 083701.
38 U. Zerweck, C. Loppacher, T. Otto, S. Grafström and L. M. Eng, *Phys. Rev. B*, 2005, **71**, 125424.
39 B. D. Terris, J. E. Stern, D. Rugar and H. J. Mamin, *Phys. Rev. Lett*., 1989, **63**, 2669.
40 H. H. Pieper, C. Barth and M. Reichling, *Appl. Phys. Lett*., 2012, **101**, 051601.
41 S. Gritschneder, Y. Namai, Y. Iwasawa and M. Reichling, *Nanotechnology*, 2005, **16**, S41.
42 S. M. F. Shahed, Y. Sainoo and T. Komeda, *Jpn. J. Appl. Phys*., 2011, **50**, 08LB05.
43 Personal communication with Fakruddin Shahed.
44 S. Gritschneder, Y. Iwasawa and M. Reichling, *Nanotechnology*, 2007, **18**, 044025.
45 S. Gritschneder and M. Reichling, *Nanotechnology*, 2007, **18**, 044024.
46 N. Nilius, S. M. Kozlov, J. F. Jerratsch, M. Baron, X. Shao, F. Viñes, S. Shaikhutdinov, K. M. Neyman and H. J. Freund, *ACS Nano*, 2012, **6**, 1126.
47 A. Munoz, A. Sominguez-Rodriguez and J. Castaing, *J. Mater. Sci*., 1994, **29**, 6207.
48 C. C. Desai, *Krist. Tech*., 1980, **15**, 809.
49 C. D. Wagner, L. E. Davis, M. V. Zeller, J. A. Taylor, R. H. Raymond and L. H. Gale, *Surf. Interface Anal*., 1981, **3**, 211.
50 K. Niihara and S. Yajima, *Bull. Chem. Soc. Jpn*., 1971, **44**, 643.
51 J. Holsa, E. Sailynoja, P. Ylha, P. Porcher, P. Deren and W. Strek, *J. Phys. Chem*., 1996, **100**, 14736.
52 S. N. Achary, B. R. Ambekar, M. D. Mathews, A. K. Tyagi and P. N. Moorthy, *Thermochim. Acta*, 1998, **320**, 239.
53 I. Levin, Q. Z. Huang, L. P. Cook and W. Wong-Ng, *Eur. J. Inorg. Chem*., 2005, 87.
54 K. T. Jacob, V. S. Saji and Y. Waseda, *Int. J. Appl. Ceram. Technol*., 2006, **3**, 312.
55 W. Finkelnburg and A. Stein, *J. Chem. Phys*., 1950, **18**, 1296.
56 J. Soria, A. Martínez-Arias, J. M. Coronado and J. C. Conesa, *Top. Catal*., 2000, **11**, 205.
57 F. Fajardie, J. F. Tempere, J. M. Manoli, G. Djega-Mariadassou and G. Blanchard, *J. Chem. Soc., Faraday Trans*., 1998, **94**, 3727.
58 F. Esch, S. Fabris, L. Zhou, T. Montini, C. Africh, P. Fornasiero, G. Comelli and R. Rosei, *Science (Washington, DC, U. S.)*, 2005, **309**, 752.
59 S. Sugiyama, K. Sogabe, T. Miyamoto, H. Hayashi and J. B. Moffat, *Catal. Lett*., 1996, **42**, 127.
60 D. Necas and P. Klapetek, *Cent. Eur. J. Phys*., 2011, **10**, 181.

